Fast Solution of Electromagnetic Scattering for 3-D Inhomogeneous Anisotropic Objects Embedded in Layered Uniaxial Media by the BCGS-FFT Method

Feng Han, *Member, IEEE*, Jianliang Zhuo, Na Liu, *Member, IEEE*, Yanhui Liu, *Member, IEEE*, Hai Liu, *Member, IEEE*, and Qing Huo Liu, *Fellow, IEEE*

***Abstract*— In this paper, the stabilized biconjugate gradient fast Fourier transform (BCGS-FFT) method is used to solve the electromagnetic scattering problem for 3-D inhomogeneous uniaxial anisotropic objects embedded in a layered uniaxial medium. The optical axis of the background medium is perpendicular to the layer boundaries. However, the optical axis of the scatterer can be rotated through any angles. The electric field integral equation (EFIE) is formulated in the layered uniaxial anisotropic background medium. The volumetric roof-top function is used for the basis function as well as the testing function. The dyadic Green's functions (DGFs) for both the electric field and the magnetic vector potential are used to solve the EFIE, and the results as well as the performance are compared. Several numerical simulations are carried out to validate the accuracy and efficiency of the proposed method. The major new contribution of this paper is to extend the BCGS-FFT method to accommodate the uniaxial anisotropy of the layered background medium. Therefore, the DGFs for the layered uniaxial medium are evaluated before solving the EFIE. In addition, the DGF for the electric field is also used to solve the 3-D scattering problem through BCGS-FFT iterations, which is different from the previous work.**

***Index Terms*— Dyadic Green's functions (DGFs), electric field integral equation (EFIE), layered media, stabilized biconjugate gradient (BCGS), uniaxial anisotropic.**

I. Introduction

SCATTERING of electromagnetic (EM) waves by arbitrary objects has attracted tremendous attention of researchers in recent years due to its wide civilian and military applications, such as high-speed circuit design [1], microwave imaging [2], [3], remote sensing [4], nondestructive testing [5], geophysical prospecting [6], and so on. The model of layered media is always taken into account in EM scattering problem, which is common in geophysical applications, such as ground penetrating radar imaging [7], or in other applications, such as printed microwave circuit analysis [8]. More realistic model also includes the anisotropy of the layered media. For example, in well-logging data processing [9], the underground structure is treated uniaxial anisotropic. Therefore, the computation of EM scattering for anisotropic objects embedded in a layered anisotropic medium is of great importance.

One of the most common methods to solve the EM scattering problem is formulating it through the integral equation (IE) [10] which can be solved mumerically. Compared with other numerical methods, such as finite-difference time domain and finite element method, the IE method has the advantage that only the computation domain enclosing the scatterers needs to be discretized. The wave propagation between the transmitters and receivers and the computation domain is described by Green's functions. For conducting scatterers, the surface IE is preferred [11]. However, the EM scattering from 3-D objects with the arbitrary inhomogeneity is typically formulated by the volume IE (VIE) [10], [12]. The VIE generally cannot be solved analytically. The method of moment (MoM) is the predominant method to solve the VIE numerically [13], [14]. However, direct matrix inverse in the MoM usually has a high computation cost [15]. Several fast solvers, such as fast multipole method [16] or multilevel fast multipole algorithm [17] have been developed to solve the EM scattering in layered media or anisotropic media. The precorrected fast Fourier transform (pFFT) method and the adaptive integral method (AIM) have been successfully adopted to solve the 3-D EM scattering in a homogeneous background medium [18], [19], a layered medium [20], and a layered uniaxial medium [21]. Both methods use the FFT acceleration to reduce the computation cost. The stabilized biconjugate gradient FFT (BCGS-FFT) method is another FFT-based solver which converges faster than the conjugate gradient (CG) [22] method and smoother than the BiCG method [23]. The pFFT and AIM use the tetrahedron mesh and have the advantage of modeling the irregular objects with a higher computation accuracy but moderate spatial sampling densities. However, the equivalent current must be projected to the auxiliary 3-D regular grid before FFT and interpolated back after FFT. This leads to the increase of the implementation cost of each iteration. By contrast, the BCGS-FFT uses a

Manuscript received April 3, 2018; revised November 15, 2018; accepted November 19, 2018. Date of publication November 28, 2018; date of current version March 5, 2019. This work was supported in part by the National Natural Science Foundation of China under Grant 41504120 and Grant 41504111 and in part by the Xiamen Science and Technology Development Funds of China under Grant 3502Z20173015. *(Corresponding authors: Hai Liu; Qing Huo Liu.)*

F. Han, J. Zhuo, and N. Liu are with the Department of Electronic Science, Institute of Electromagnetics and Acoustics, Xiamen University, Xiamen 361008, China (e-mail: feng.han@xmu.edu.cn).

Y. Liu is with the Department of Electronic Science, Institute of Electromagnetics and Acoustics, Xiamen University, Xiamen 361005, China, and also with the Global Big Data Technologies Centre, University of Technology Sydney, Ultimo, NSW 2007, Australia.

H. Liu is with the School of Civil Engineering, Guangzhou University, Guangzhou 510006, China (e-mail: hliu@gzhu.edu.cn).

Q. H. Liu is with the Department of Electrical and Computer Engineering, Duke University, Durham, NC 27708 USA (e-mail: qhliu@duke.edu).

Color versions of one or more of the figures in this paper are available online at http://ieeexplore.ieee.org.

Digital Object Identifier 10.1109/TAP.2018.2883682

hexahedron mesh in the discretization of VIE, which facilitates the direct application of FFT. Meanwhile, the BCGS-FFT can be easily combined with inversion algorithms to reconstruct the dielectric constants of the scatterers. Several papers have been published regarding the reliable combination of BCGS-FFT and inversion algorithms [24], [25]. Of course, the simplicity of the implementation of the BCGS-FFT comes at a cost of higher spatial sampling densities, especially when the scattering objects are irregular. The pFFT/AIM and the BCGS-FFT have their own advantages and disadvantages. Therefore, the choice of the optimal method is problem-dependent, and we focus on the application of the BCGS-FFT in this paper.

Previously, a lot of research work has been done regarding using the BCGS-FFT method to solve the VIE for isotropic or anisotropic scatterers embedded in homogeneous or planarly layered media. At the beginning, it was adopted to solve the electric field IE (EFIE) iteratively and calculate the total fields in the computation domain [15], [26]. Later, the permeability contrast was added, and thus, the magnetic field IE was combined with the EFIE to form the coupled field VIE (CFVIE) which can also be solved by the BCGS-FFT [27]. Recently, new progress was made and the anisotropy of the scatterer was considered. Yu *et al.* [28], [29] applied the BCGS-FFT to solve the scattering problem for anisotropic magnetodielectric scatterers embedded in a homogeneous medium. Meanwhile, the mixed-order basis functions were used to expand the flux and vector potentials. Jia *et al.* [30] later extended this work furthermore and considered the layered background medium. However, in all this work, the background medium was assumed to be isotropic, for both homogeneous and layered models. Although there was also recent work dealing with the EM scattering in a layered uniaxial background medium, different methods were taken instead of BCGS-FFT. Yang and Yilmaz [21] solved the EM scattering from arbitrary anisotropic scatterers buried in a layered uniaxial media by AIM. Zhong *et al.* [31] adopted the Padua points together with the windowing technique to solve the EM scattering in a layered uniaxial media with its optical axis parallel to the layer interface.

In this paper, we adopt the BCGS-FFT fast solver to compute the EM scattering in a layered uniaxial anisotropic background medium. The optical axis of the background is assumed to be perpendicular to the layer interface. But the optical axis of the scatterer can be rotated in an arbitrary direction. In addition, besides using the dyadic Green's function (DGF) for the magnetic vector potential, we also use the DGF for the electric field to solve the EFIE. Both results are compared with the numerical simulation from the commercial software COMSOL to validate the accuracy and efficiency. Compared with the implementation in an isotropic background medium, the BCGS iteration for the uniaxial anisotropic background medium has different coefficients and interactions between the DGFs and equivalent current, which are generated from the weak forms of the EFIE for anisotropic scatterers embedded in a layered uniaxial medium. Finally, it should be noted that the time dependence $e^{j\omega t}$ is used throughout this paper.

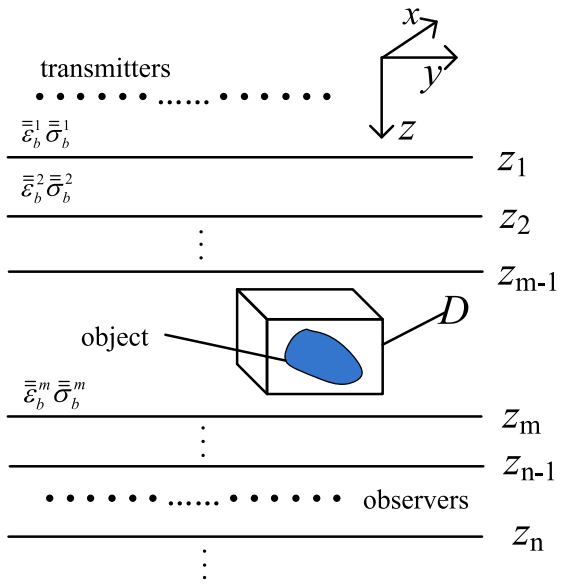

Fig. 1. Typical configuration for electromagnetic scattering in a planarly layered uniaxial anisotropic medium.

The organization of this paper is as follows. In Section II, the mathematical formulation of the EFIE for 3-D anisotropic scatterers embedded in a layered uniaxial anisotropic medium is given. Evaluation of the DGFs for the magnetic vector potential and the electric field is briefly described. In addition, the FFT acceleration of the convolution as well as the correlation between DGFs and the equivalent electric current are presented. In Section III, several numerical simulations are performed and the results are compared with the COMSOL simulation results. Finally, in Section IV, conclusions are drawn and a discussion is presented.

II. Formulation

The objective of this paper is to solve the scattering problem of inhomogeneous uniaxial anisotropic objects embedded in a layered uniaxial anisotropic background medium with the optic axis in the z direction. The typical configuration for the EM scattering is shown in Fig. 1. We assume the object is completely embedded in the mth layer, and do not consider magnetic materials, i.e., the permeability is the same as that of free space μ_0. The relative permittivity and conductivity tensors of the ith layer are written as

$$\bar{\bar{\varepsilon}}_b^i = \begin{bmatrix} \varepsilon_{xb}^i & 0 & 0 \\ 0 & \varepsilon_{xb}^i & 0 \\ 0 & 0 & \varepsilon_{zb}^i \end{bmatrix}, \quad \bar{\bar{\sigma}}_b^i = \begin{bmatrix} \sigma_{xb}^i & 0 & 0 \\ 0 & \sigma_{xb}^i & 0 \\ 0 & 0 & \sigma_{zb}^i \end{bmatrix} \tag{1}$$

where the subscript b means the background. The relative complex tensor permittivity of the ith layer is defined as

$$\bar{\bar{\epsilon}}_b^i = \bar{\bar{\varepsilon}}_b^i + \frac{\bar{\bar{\sigma}}_b^i}{j\omega\varepsilon_0} \tag{2}$$

where ω is the angular frequency of the EM wave. The relative permittivity and conductivity tensors of the object which can be embedded in any layer are written as

$$\bar{\bar{\varepsilon}}_s = \begin{bmatrix} \varepsilon_{xs} & 0 & 0 \\ 0 & \varepsilon_{xs} & 0 \\ 0 & 0 & \varepsilon_{zs} \end{bmatrix}, \quad \bar{\bar{\sigma}}_s = \begin{bmatrix} \sigma_{xs} & 0 & 0 \\ 0 & \sigma_{xs} & 0 \\ 0 & 0 & \sigma_{zs} \end{bmatrix}. \tag{3}$$

The relative complex tensor permittivity of the object is defined as

$$\overline{\overline{\epsilon}}_s = \overline{\overline{\varepsilon}}_s + \frac{\overline{\overline{\sigma}}_s}{j\omega\varepsilon_0}. \tag{4}$$

A. Electric Field Integral Equation in a Layered Uniaxial Anisotropic Medium

According to the volume equivalence principle [32], the scattered electric field $\mathbf{E}^s$ is equal to the field radiated by the equivalent electric current source $\mathbf{J}_{eq}$ inside the anisotropic object which can be expressed as

$$\mathbf{J}_{eq}(\mathbf{r}) = j\omega\overline{\overline{\chi}}(\mathbf{r})\mathbf{D}_{tot}(\mathbf{r}) \tag{5}$$

where the tensor

$$\overline{\overline{\chi}}(\mathbf{r}) = [\overline{\overline{\epsilon}}(\mathbf{r}) - \overline{\overline{\epsilon}}_b]\overline{\overline{\epsilon}}^{-1}(\mathbf{r}) \tag{6}$$

is the dielectric contrast function and $\overline{\overline{\epsilon}}(\mathbf{r})$ is the relative complex tensor permittivity at any point $\mathbf{r}$ in the whole space. $\mathbf{D}_{tot} = \overline{\overline{\epsilon}}\varepsilon_0\mathbf{E}_{tot}$ is the total electric flux density. If the DGF for the magnetic vector potential $\mathbf{A}$ (DGFA) is adopted, the scattered electric field in a layered uniaxial anisotropic medium can be written as [33]

$$\mathbf{E}^n_{sct}(\mathbf{r}) = -j\omega\left(1 + \frac{1}{k_0^2\epsilon^n_{xb}}\nabla\nabla\cdot\right)\mathbf{A}^n(\mathbf{r}) \tag{7}$$

where $k_0 = \omega\sqrt{\varepsilon_0\mu_0}$ is the wavenumber in the free space. The magnetic vector potential $\mathbf{A}^n$ can be calculated as

$$\mathbf{A}^n(\mathbf{r}) = j\omega\mu_0\int_D \overline{\overline{\mathbf{G}}}^{nm}_{\mathbf{A}}(\mathbf{r},\mathbf{r}')\cdot\overline{\overline{\chi}}(\mathbf{r}')\mathbf{D}^m_{tot}(\mathbf{r}')d\mathbf{r}' \tag{8}$$

where $\overline{\overline{\mathbf{G}}}^{nm}_{\mathbf{A}}$ is the layered DGFA connecting the equivalent electric current source in the mth layer and the magnetic vector potential $\mathbf{A}$ in the nth layer, and D is the computation domain enclosing the scatterers and located in the mth layer. Alternatively, if the DGF for the electric field $\mathbf{E}$ (DGFE) is adopted, the scattered electric field can be written more compactly as

$$\mathbf{E}^n_{sct}(\mathbf{r}) = \omega^2\mu_0\int_D \overline{\overline{\mathbf{G}}}^{nm}_{\mathbf{E}}(\mathbf{r},\mathbf{r}')\cdot\overline{\overline{\chi}}(\mathbf{r}')\mathbf{D}^m_{tot}(\mathbf{r}')d\mathbf{r}' \tag{9}$$

where $\overline{\overline{\mathbf{G}}}^{nm}_{\mathbf{E}}$ is the layered DGFE. In virtue of (7) and (8), it is easy to formulate the EFIE based on DGFA as

$$\mathbf{E}^n_{inc}(\mathbf{r}) = \mathbf{E}^n_{tot}(\mathbf{r}) - \mathbf{E}^n_{sct}(\mathbf{r}) = \overline{\overline{\epsilon}}^{-1}(\mathbf{r})\frac{\mathbf{D}^n_{tot}(\mathbf{r})}{\varepsilon_0} - \left(\omega^2\mu_0 + \frac{1}{\varepsilon_0\epsilon^n_{xb}}\nabla\nabla\cdot\right)\int_D \overline{\overline{\mathbf{G}}}^{nm}_{\mathbf{A}}(\mathbf{r},\mathbf{r}')\cdot\overline{\overline{\chi}}(\mathbf{r}')\mathbf{D}^m_{tot}(\mathbf{r}')d\mathbf{r}' \tag{10}$$

where $\mathbf{E}^n_{inc}$ is the incident electric field evaluated in the nth layer when the scatterers are absent. The flux $\mathbf{D}_{tot}$ is used to replace $\mathbf{E}_{tot}$ because the divergence conforming basis function will be adopted. If we choose the DGFE, the EFIE can be written as

$$\mathbf{E}^n_{inc}(\mathbf{r}) = \overline{\overline{\epsilon}}^{-1}(\mathbf{r})\frac{\mathbf{D}^n_{tot}(\mathbf{r})}{\varepsilon_0} - \omega^2\mu_0\int_D \overline{\overline{\mathbf{G}}}^{nm}_{\mathbf{E}}(\mathbf{r},\mathbf{r}')\cdot\overline{\overline{\chi}}(\mathbf{r}')\mathbf{D}^m_{tot}(\mathbf{r}')d\mathbf{r}'. \tag{11}$$

Once the total flux $\mathbf{D}_{tot}$ in the nth layer is acquired, the scattered fields anywhere can be obtained through (7) and (8) or (9).

B. Optical Axis Rotation of the Uniaxial Scatterer

If the optical axis of the scatterer is not aligned with that of the background medium, i.e., not in the z direction, successive rotations can be carried out to align them. In this paper, we use the rotation rule suggested in [34]. It is assumed that the local coordinate system of the scatterer can be aligned to the coordinate system of the background medium following two successive rotations with the angle ψ_1 and ψ_2. They correspond to the anticlockwise rotations about the local x axis and z axis of the scatterer coordinate system, respectively. After rotation, the new dielectric tensors $\overline{\overline{\varepsilon}}'_s$ and $\overline{\overline{\sigma}}'_s$ become full tensors instead of diagonal ones. The mathematical relationships between $\overline{\overline{\varepsilon}}'_s$ and $\overline{\overline{\varepsilon}}_s$, as well as $\overline{\overline{\sigma}}'_s$ and $\overline{\overline{\sigma}}_s$ can be found in [34].

Consequently, the contrast function $\overline{\overline{\chi}}$ in (5) and (6) also becomes a full tensor. Equations (7)–(11) keep valid when the full tensors $\overline{\overline{\chi}}$ and $\overline{\overline{\epsilon}}$ are used.

C. Evaluation of the Dyadic Green's Functions in a Layered Medium

Equations (10) and (11) are valid everywhere. When we solve the EFIEs, it is convenient to let the field point $\mathbf{r} \in D$, i.e., $n = m$ [26]. In this way, in a layered medium, $\overline{\overline{\mathbf{G}}}^{mm}_{\mathbf{A}}$ in (10) can be decomposed into two terms as

$$\overline{\overline{\mathbf{G}}}^{mm}_{\mathbf{A}}(\mathbf{r},\mathbf{r}') = \overline{\overline{\mathbf{G}}}^{d}_{\mathbf{A}}(\mathbf{r},\mathbf{r}') + \overline{\overline{\mathbf{G}}}^{rt}_{\mathbf{A}}(\mathbf{r},\mathbf{r}') \tag{12}$$

where $\overline{\overline{\mathbf{G}}}^{d}_{\mathbf{A}}$ denotes the contribution from the direct EM wave propagating from the source point $\mathbf{r}'$ to the field point $\mathbf{r}$ inside the mth layer, and $\overline{\overline{\mathbf{G}}}^{rt}_{\mathbf{A}}$ denotes the contribution from the reflected and transmitted EM waves in the layer boundaries. In a similar way, the $\overline{\overline{\mathbf{G}}}^{mm}_{\mathbf{E}}$ in (11) can also be decomposed into two terms as

$$\overline{\overline{\mathbf{G}}}^{mm}_{\mathbf{E}}(\mathbf{r},\mathbf{r}') = \overline{\overline{\mathbf{G}}}^{d}_{\mathbf{E}}(\mathbf{r},\mathbf{r}') + \overline{\overline{\mathbf{G}}}^{rt}_{\mathbf{E}}(\mathbf{r},\mathbf{r}'). \tag{13}$$

1) DGFs in a Layered Isotropic Medium: If the layered medium is isotropic, both $\overline{\overline{\mathbf{G}}}^{d}_{\mathbf{A}}$ and $\overline{\overline{\mathbf{G}}}^{d}_{\mathbf{E}}$ have the analytic expressions. The $\overline{\overline{\mathbf{G}}}^{d}_{\mathbf{A}}$ can be written as

$$\overline{\overline{\mathbf{G}}}^{d}_{\mathbf{A}}(\mathbf{r},\mathbf{r}') = g(\mathbf{r},\mathbf{r}')\overline{\overline{\mathbf{I}}} \tag{14}$$

where $\overline{\overline{\mathbf{I}}}$ is the unit tensor. And, $g(\mathbf{r},\mathbf{r}')$ is the scalar Green's function which is expressed as

$$g(\mathbf{r},\mathbf{r}') = \frac{e^{-jk_m|\mathbf{r}-\mathbf{r}'|}}{4\pi|\mathbf{r}-\mathbf{r}'|} \tag{15}$$

where k_m is the wavenumber in the mth layer. The $\overline{\overline{\mathbf{G}}}^{d}_{\mathbf{E}}$ can be expressed as

$$\overline{\overline{\mathbf{G}}}^{d}_{\mathbf{E}}(\mathbf{r},\mathbf{r}') = \left[\overline{\overline{\mathbf{I}}} + \frac{1}{k_m^2}\nabla\nabla\cdot\right]\overline{\overline{\mathbf{G}}}^{d}_{\mathbf{A}}(\mathbf{r},\mathbf{r}') = \left[\overline{\overline{\mathbf{I}}} + \frac{1}{k_m^2}\nabla\nabla\right]g(\mathbf{r},\mathbf{r}'). \tag{16}$$

However, both $\overline{\overline{\mathbf{G}}}^{rt}_{\mathbf{A}}$ and $\overline{\overline{\mathbf{G}}}^{rt}_{\mathbf{E}}$ have no explicit analytic expression. They are usually computed through numerical Sommerfeld integration. A detailed derivation of $\overline{\overline{\mathbf{G}}}_{\mathbf{A}}$ and $\overline{\overline{\mathbf{G}}}_{\mathbf{E}}$ can be found in [33].

2) DGFs in a Layered Uniaxial Anisotropic Medium: When the layered medium is uniaxial anisotropic, both $\overline{\overline{\mathbf{G}}}^{d}_{\mathbf{E}}$ and $\overline{\overline{\mathbf{G}}}^{d}_{\mathbf{A}}$ can be evaluated numerically through the Sommerfeld integration in a straightforward way [33], [35], or computed with complicated analytic expressions [36], [37]. However, both $\overline{\overline{\mathbf{G}}}^{rt}_{\mathbf{A}}$ and $\overline{\overline{\mathbf{G}}}^{rt}_{\mathbf{E}}$ also must be computed through the numerical Sommerfeld integration [33].

3) Singularities of DGFs: As shown in (8) and (9), the magnetic vector potential $\mathbf{A}$ and the scattered electric field are generated by the equivalent electric current in the computation domain D. As mentioned above, we let $\mathbf{r} \in D$ when solving the EFIE. Therefore, it is inevitable to evaluate the DGFs when $\mathbf{r} = \mathbf{r}'$. It is clear $\overline{\overline{\mathbf{G}}}^{rt}_{\mathbf{A}}$ and $\overline{\overline{\mathbf{G}}}^{rt}_{\mathbf{E}}$ have no singularity and can be calculated by the Sommerfeld integration. In the isotropic medium, $\overline{\overline{\mathbf{G}}}^{d}_{\mathbf{A}}$, when $\mathbf{r} = \mathbf{r}'$ also has no singularity and its contribution from a unit current density in a discretized cubic cell to the magnetic vector potential $\mathbf{A}$ in the cell center can be approximated by [38]

$$\int_C \overline{\overline{\mathbf{G}}}^{d}_{\mathbf{A}}(\mathbf{r},\mathbf{r}')d\mathbf{r}' = \int_0^{4\pi} d\Omega \int_0^a \overline{\overline{\mathbf{G}}}^{d}_{\mathbf{A}}(0,r')r'^2 dr' = \frac{1}{k_m^2}[(1+jk_m a)e^{-jk_m a}-1]\overline{\overline{\mathbf{I}}} \quad (17)$$

where C represents the discretized cell region. However, $\overline{\overline{\mathbf{G}}}^{d}_{\mathbf{E}}$ when $\mathbf{r} = \mathbf{r}'$ has singularity and its contribution from a unit current density in a discretized cubic cell to the electric field in the cell center can be approximated by [39], [40]

$$\int_C \overline{\overline{\mathbf{G}}}^{d}_{\mathbf{E}}(\mathbf{r},\mathbf{r}')d\mathbf{r}' = \int_0^{4\pi} d\Omega \int_0^a \overline{\overline{\mathbf{G}}}^{d}_{\mathbf{E}}(0,r')r'^2 dr' = \frac{2}{3k_m^2}[(1+jk_m a)e^{-jk_m a}-1]\overline{\overline{\mathbf{I}}} - \frac{1}{3k_m^2}\overline{\overline{\mathbf{I}}}. \quad (18)$$

In (17) and (18), a is the radius of the equivalent sphere of the cubic cell, i.e., $\Delta x \times \Delta y \times \Delta z = \Delta x^3 = (4\pi/3)a^3$. Here, Δx, Δy, and Δz are the discretized cell sizes in three directions, respectively. The second term in the right-hand side of (18) is the contribution of the singularity when $\mathbf{r} = \mathbf{r}'$ [41]. Equations (17) and (18) are only valid when the medium is isotropic. When the background medium is uniaxial anisotropic, the above integral can only be estimated numerically. It is assumed that the field point $\mathbf{r}$ is located in the center of the cell, and we uniformly discretize it to several smaller cells and put the source points $\mathbf{r}'$ in the centers of these smaller cells. The DGF for each source point is evaluated individually and the arithmetic mean is calculated later. The second term in the right-hand side of (18) should be modified according to [42] for a uniaxial anisotropic medium.

D. Interactions Between DGFs and the Equivalent Current

As shown in (8) and (9), the interactions between the DGFs and the equivalent current $\mathbf{J}_{eq}$ are 3-D volume integration. Since the field point $\mathbf{r}$ is also in the domain D when the EFIE is discretized and solved iteratively, direct computation of the integration is time consuming.

In homogeneous media, the integration in (8) and (9) can be treated as convolution since the DGF can be written as

$$\overline{\overline{\mathbf{G}}}(\mathbf{r},\mathbf{r}') = \overline{\overline{\mathbf{G}}}(\mathbf{r}-\mathbf{r}') \quad (19)$$

where $\overline{\overline{\mathbf{G}}}$ can either be $\overline{\overline{\mathbf{G}}}_{\mathbf{A}}$ or $\overline{\overline{\mathbf{G}}}_{\mathbf{E}}$. The convolution can be easily accelerated by the FFT algorithm. However, in layered media, (19) no longer holds due to the reflection and the transmission in the layer boundaries, and thus, the FFT cannot be directly applied. Fortunately, the DGF can be decomposed into "minus" and "plus" parts and expressed as [10], [26], [33]

$$\overline{\overline{\mathbf{G}}}(\mathbf{r},\mathbf{r}') = \overline{\overline{\mathbf{G}}}_m(x-x', y-y', z-z') + \overline{\overline{\mathbf{G}}}_p(x-x', y-y', z+z') \quad (20)$$

where the subscript m means "minus" while p means "plus." It should be noted that, the "plus" is only for the z direction. $\overline{\overline{\mathbf{G}}}_p$ keeps "minus" in the xy plane. Therefore, the interaction between $\overline{\overline{\mathbf{G}}}_m$ and the equivalent current $\mathbf{J}_{eq}$ is convolution in all the three directions and can be readily accelerated by the 3-D FFT. The interaction between $\overline{\overline{\mathbf{G}}}_p$ and $\mathbf{J}_{eq}$ is convolution in the xy plane but correlation in the z direction, and can be accelerated by the 2-D FFT in the xy plane followed by the complex conjugate operation as well as 1-D FFT in the z direction. Finally, we want to emphasize that $\overline{\overline{\mathbf{G}}}^{d}_{\mathbf{A}}$ and $\overline{\overline{\mathbf{G}}}^{d}_{\mathbf{E}}$ discussed in last subsection belong to the "minus" part.

E. Discretization and the Weak Forms

In order to solve the EFIEs in (10) and (11) numerically, we discretize them at first to obtain the linear systems. In this paper, we use the similar method presented in [38]. Both the flux and the magnetic vector potential are expanded by the first order divergence conforming basis function, i.e., the 3-D volumetric rooftop basis function

$$D^{n(q)}_{tot}(\mathbf{r}) = \varepsilon_0 \sum_{\mathbf{i}} d^{(q)}_{\mathbf{i}} \psi^{(q)}_{\mathbf{i}}(\mathbf{r}) \quad (21)$$

$$A^{n(q)}(\mathbf{r}) = \sum_{\mathbf{i}} A^{(q)}_{\mathbf{i}} \psi^{(q)}_{\mathbf{i}}(\mathbf{r}) \quad (22)$$

where $q = 1, 2$, and 3 are corresponding to $\hat{x}$, $\hat{y}$, and $\hat{z}$ three components, respectively, and $\mathbf{i} = \{I, J, K\}$ are the indexes of the discretized cells for three components, respectively. $d^{(q)}_{\mathbf{i}}$ and $A^{(q)}_{\mathbf{i}}$ are the expansion coefficients for $D^{(q)}$ and $A^{(q)}$, respectively, and $\psi^{(q)}$ is the basis function with the detailed expression given in [38]. After expanding the incident field in a similar way as in (21) and (22)

$$E^{n(q)}_{inc}(\mathbf{r}) = \sum_{\mathbf{i}} E^{i,(q)}_{\mathbf{i}} \psi^{(q)}_{\mathbf{i}}(\mathbf{r}) \quad (23)$$

we then test both sides of the EFIE (10) with the same rooftop function $\psi^{(p)}_{\mathbf{m}}(\mathbf{r})$ with $p = 1, 2$, and 3 for three orthogonal directions, and $\mathbf{m} = \{M, N, P\}$ the indexes of the discretized cells, and can obtain the domain-integral weak form of the EFIE (10) which is different from that given in [38] due to the

layered anisotropic background medium and the anisotropic scatterers. It can be compactly written as

$$e_{\mathbf{m}}^{i,(p)}=\sum_{\mathbf{i}}\sum_{q=1}^{3} d_{\mathbf{i}}^{(q)} u_{\mathbf{m};\mathbf{i}}^{(p,q)}+A_{\mathbf{i}}^{(q)}\left[j\omega v_{\mathbf{m};\mathbf{i}}^{(p,q)}-\frac{j}{\omega\varepsilon_0\mu_0\epsilon_{xb}^{n}} w_{\mathbf{m};\mathbf{i}}^{(p,q)}\right] \tag{24}$$

where

$$u_{\mathbf{m};\mathbf{i}}^{(p,q)}=\int_D \psi_{\mathbf{m}}^{(p)}(\mathbf{r})\overline{\overline{\epsilon}}^{-1}(\mathbf{r})\psi_{\mathbf{i}}^{(q)}(\mathbf{r})d\mathbf{r}. \tag{25}$$

The expressions for $e_{\mathbf{m}}^{i,(p)}$, $v_{\mathbf{m};\mathbf{i}}^{(p,q)}$, and $w_{\mathbf{m};\mathbf{i}}^{(p,q)}$ are the same as those in the isotropic case and given in [38]. $A_{\mathbf{i}}^{(q)}$ is one component of $\mathbf{A_i}$ which can be computed as

$$\mathbf{A_i}=j\omega\varepsilon_0\mu_0\Delta V\cdot\sum_{\mathbf{i}'}\overline{\overline{\mathbf{G}}}_{\mathbf{A}}(\mathbf{i},\mathbf{i}')\cdot(\overline{\overline{\chi}}_{\mathbf{i}'}\cdot\mathbf{d}_{\mathbf{i}'}) \tag{26}$$

where $\mathbf{i}=\{I,J,K\}$ are indexes for field point cells while $\mathbf{i}'=\{I',J',K'\}$ are indexes for equivalent current cells. $\Delta V=\Delta x\Delta y\Delta z$ is the discretized cell volume. $\mathbf{d}_{\mathbf{i}'}$ is a vector containing $d_{I',J',K'}^{(q)}$ with $q=1,2$, and 3. Although $\overline{\overline{\chi}}_{\mathbf{i}'}$ becomes a full tensor when the optical axis is rotated, the equivalent current term $\overline{\overline{\chi}}_{\mathbf{i}'}\cdot\mathbf{d}_{\mathbf{i}'}$ keeps a vector. Its interaction with the DGFA $\overline{\overline{\mathbf{G}}}_{\mathbf{A}}$ is a discrete convolution in the xy plane but should be decomposed into convolution and correlation in the z direction as mentioned in last subsection. The computation of $\mathbf{A_i}$ in (26) is totally different from the computation of $A_{I,J,K}^{(q)}$ presented in [38] due to the dyad $\overline{\overline{\mathbf{G}}}_{\mathbf{A}}$ and the full tensor $\overline{\overline{\chi}}$.

Since both the basis and testing functions $\psi^{(p)}$ and $\psi^{(q)}$ are rooftop functions, it is not difficult to perform the integrals in $u_{\mathbf{m};\mathbf{i}}^{(p,q)}$, $v_{\mathbf{m};\mathbf{i}}^{(p,q)}$, and $w_{\mathbf{m};\mathbf{i}}^{(p,q)}$ in (24). In this way, we can obtain the complete discretized weak form of (24) which can be compactly written as

$$\begin{aligned} e_{\mathbf{m}}^{i,(p)} &= \sum_{q=p}^{p+2}\sum_{l=1}^{3}\mathbf{S}_{\mathbf{m},l}^{(q)}\left[d_{\mathbf{m}+\hat{x}_p(l-2)}^{(q)}+(1-\delta_{p,q})d_{\mathbf{m}+\hat{x}_p(l-2)+\hat{x}_q}^{(q)}\right] \\ &\quad+\sum_{l=1}^{3}\mathbf{Q}_{\mathbf{m},l}^{(p)}A_{\mathbf{m}+\hat{x}_p(l-2)}^{(p)}+\sum_{i=1}^{2}\sum_{j=1}^{2}\left[\mathbf{T}_{ij}^{(p+1)}A_{\mathbf{m}+\hat{x}_p(i-2)+\hat{x}_{p+2}(j-1)}^{(p+2)}\right. \\ &\quad\left.+\mathbf{T}_{ij}^{(p+2)}A_{\mathbf{m}+\hat{x}_p(i-2)+\hat{x}_{p+1}(j-1)}^{(p+1)}\right] \end{aligned} \tag{27}$$

where $p,q,p+1,q+1,p+2$, and $q+2$ are cyclic indexes with the period of 3, and $\delta_{p,q}$ is the Kronecker symbol. $\hat{x}_p$ is the unit vector in the pth direction. $\mathbf{S}_{\mathbf{m},l}^{(q)}$ is the lth component of the vector $\mathbf{S}_{\mathbf{m}}^{(q)}$ which is given as

$$\mathbf{S}_{\mathbf{m}}^{(q)}=\frac{\Delta x\Delta y\Delta z}{6}\begin{Bmatrix}\overline{\overline{\epsilon}}_{\mathbf{m}-\hat{x}_p,pp}^{-1}\\ 2\overline{\overline{\epsilon}}_{\mathbf{m}-\hat{x}_p,pp}^{-1}+2\overline{\overline{\epsilon}}_{\mathbf{m},pp}^{-1}\\ \overline{\overline{\epsilon}}_{\mathbf{m},pp}^{-1}\end{Bmatrix} \tag{28}$$

when $q=p$, but

$$\mathbf{S}_{\mathbf{m}}^{(q)}=\frac{\Delta x\Delta y\Delta z}{4}\begin{Bmatrix}\overline{\overline{\epsilon}}_{\mathbf{m}-\hat{x}_p,pq}^{-1}\\ \overline{\overline{\epsilon}}_{\mathbf{m},pq}^{-1}\\ 0\end{Bmatrix} \tag{29}$$

when $q=p+1$ or $q=p+2$. In (28) and (29), $\overline{\overline{\epsilon}}_{pq}^{-1}$ is the pq component of the full tensor $\overline{\overline{\epsilon}}^{-1}$. $\mathbf{Q}_{\mathbf{m},l}^{(p)}$ is the lth component of the vector $\mathbf{Q}_{\mathbf{m}}^{(p)}$ which is given as

$$\mathbf{Q}_{\mathbf{m}}^{(p)}=\Delta V\left\{\frac{j\omega}{6}\begin{pmatrix}1\\4\\1\end{pmatrix}-\frac{j}{\omega\varepsilon_0\mu_0\epsilon_{xb}^{n}(\Delta x_p)^2}\begin{pmatrix}-1\\2\\-1\end{pmatrix}\right\} \tag{30}$$

where $\Delta x_1=\Delta x$, $\Delta x_2=\Delta y$, and $\Delta x_3=\Delta z$. Similarly, $\mathbf{T}_{ij}^{(p)}$ is the ij component of the matrix $\mathbf{T}^{(p)}$ which is given as

$$\mathbf{T}^{(p)}=-\frac{j\Delta x_p}{\omega\varepsilon_0\mu_0\epsilon_{xb}^{n}}\begin{Bmatrix}-1 & 1\\ 1 & -1\end{Bmatrix}. \tag{31}$$

Compared with the weak forms given in [38], the major difference shown in (27) arises from the discretization for $\overline{\overline{\epsilon}}^{-1}(\mathbf{D}_{tot}/\varepsilon_0)$. When the optical axis of the scatterer is rotated, both the contrast $\overline{\overline{\chi}}$ and $\overline{\overline{\epsilon}}^{-1}$ become full tensors, and thus, the cross polarization terms show up after $(1-\delta_{p,q})$ in (27). In addition, the coefficients in (30) and (31) are also completely different from those given in [38] due to the anisotropy of the background medium and scatterers.

Compared with (24), the domain-integral weak form of (11) is simpler due to the absence of the operator $\nabla\nabla$, and it can be compactly written as

$$e_{\mathbf{m}}^{i,(p)}=\sum_{\mathbf{i}}\sum_{q=1}^{3} d_{\mathbf{i}}^{(q)} u_{\mathbf{m};\mathbf{i}}^{(p,q)}-E_{\mathbf{i}}^{s,(q)} v_{\mathbf{m};\mathbf{i}}^{(p,q)} \tag{32}$$

where $u_{\mathbf{m};\mathbf{i}}^{(p,q)}$ and $v_{\mathbf{m};\mathbf{i}}^{(p,q)}$ are the same as those used for (24). $E_{\mathbf{i}}^{s,(q)}$ can be obtained by discretizing (9) and it comes to a similar formula as (26). By taking a similar procedure shown above, we can obtain the complete weak form of (11) which is simpler than (27) and will not be presented here.

In the discretized EFIE of (10) or (11), the coefficients $d^{(q)}$ are the unknowns to be solved by the BCGS iteration. The convolution and correlation operation in (10) and (11) is transformed into discrete convolution and correlation. Therefore, in each iteration, the FFT is performed to accelerate the integration in the weak forms of (10) and (11). In this way, the time complexity of the BCGS is decreased from $O(KN^2)$ to $O(KN\log N)$, where K is the iteration number and N is the number of unknowns in the discretized computation domain. Compared with the BCGS-FFT implementation in isotropic background media, the coefficients of the weak forms of the EFIEs and the interactions between the DGFs and the equivalent current are the major difference in anisotropic media.

III. Numerical Results

In this section, we simulate the EM scattering by the three canonical 3-D uniaxial anisotropic objects embedded in a layered uniaxial anisotropic media to validate the method given in last section. The BCGS-FFT results are compared with the numerical simulation results from the commercial software COMSOL. For convenience, several basic parameters are set the same, and are no longer repeated for each case. The source

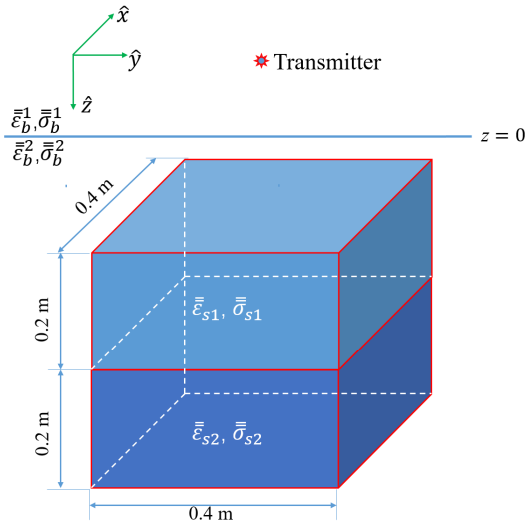

Fig. 2. Configuration of a two-layer cubic scatterer with the dimension of 0.4 m × 0.4 m × 0.4 m embedded in a half-space uniaxial anisotropic background medium.

is a unit electric dipole, operating at 1 GHz and polarized by (1, 1, 1). In order to mimic the EM radiation from antennas, we treat the first layer as air and put both the transmitter and the receiver array in this layer. The stop criterion of the BCGS iteration residual errors for all cases are set to be 10^{-5}. The EM scattering results are demonstrated below. In the first three examples, the optical axis of the scatterer is aligned with that of the background medium. In the fourth case, they are not overlapped anymore, and the rotation is conducted to compute the full tensors of the dielectric parameters of the scatterer before the BCGS iteration. And, in the fifth case, we compare the computation accuracy, time, and memory consumption of the anisotropic EM scattering with the isotropic EM scattering. All cases and COMSOL simulations presented in this paper are performed on a workstation with 20-cores Xeon E2650 v3 2.3 GHz CPU and 512 GB RAM.

A. Two-Layer Uniaxial Anisotropic Cube Embedded in a Half-space Background

Fig. 2 shows the configuration of a two-layer cube with the size of 0.4 m × 0.4 m × 0.4 m located at the bottom layer of a half-space background. The top layer of the background is air, i.e., $\overline{\overline{\varepsilon}}_b^1 = \overline{\overline{\mathbf{I}}}$ and $\overline{\overline{\sigma}}_b^1 = 0$. The boundary is at $z = 0$. The bottom layer has the dielectric parameters

$$\overline{\overline{\varepsilon}}_b^2 = diag\{2.0, 2.0, 1.5\}, \overline{\overline{\sigma}}_b^2 = diag\{1, 1, 2\} \text{ mS/m}. \quad (33)$$

Two layers of the scatterer have the same thickness 0.2 m, and the dielectric parameters are

$$\overline{\overline{\varepsilon}}_{s1} = diag\{4.0, 4.0, 3.5\}, \overline{\overline{\sigma}}_{s1} = diag\{2, 2, 3\} \text{ mS/m} \quad (34)$$

and

$$\overline{\overline{\varepsilon}}_{s2} = diag\{1.5, 1.5, 2.0\}, \overline{\overline{\sigma}}_{s2} = diag\{3, 3, 4\} \text{ mS/m}. \quad (35)$$

The center of the two-layer cube is at (0, 0, 0.4) m. The electric dipole is located at (0, 0, −0.1) m. The computation

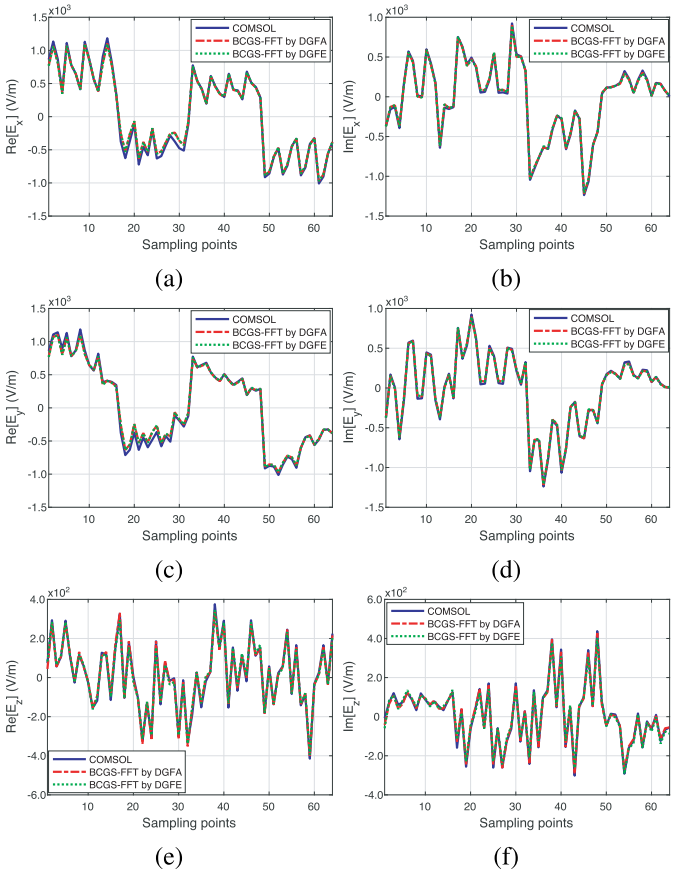

Fig. 3. Comparisons of the total electric fields inside the cube computed by the BCGS-FFT through DGFA as well as DGFE and simulated by the COMSOL. (a) Real part of E_x. (b) Imaginary part of E_x. (c) Real part of E_y. (d) Imaginary part of E_y. (e) Real part of E_z. (f) Imaginary part of E_z.

domain of BCGS-FFT has the same size as that of the scatterer, and is discretized into 50^3 cubic cells with 375 thousand unknowns. Thus, the sampling density (SD) is larger than 18 points per wavelength (PPW) inside the cube. In the COMSOL simulation model, the computation domain is 0.6 m × 0.6 m × 0.6 m which includes the electric dipole source, and the thickness of the perfect match layers (PMLs) is set as 0.075 m on the periphery of the computation domain. In order to maintain the COMSOL simulation accuracy, we set the mesh sizes as EXTRA FINE. The mesh and PML settings are the same for all the COMOSL simulations presented in this paper.

At first, let us verify the total electric fields inside the two-layer anisotropic cube and study the convergence of the BCGS iteration through DGFA and DGFE. Fig. 3 shows the comparisons of the total fields solved by the BCGS-FFT method and the COMSOL simulations. Here, we only pick 64 uniformly distributed sampling points inside the object for comparisons. We can see that all the three components of the total electric fields solved by the BCGS-FFT method through DGFA as well as DGFE match well with the COMSOL simulated results. By treating the COMSOL simulated results as a reference, we quantitatively define the relative error as

$$err_F^g = \frac{\|\mathbf{F}_b^g - \mathbf{F}_c\|}{\|\mathbf{F}_c\|} \quad (36)$$

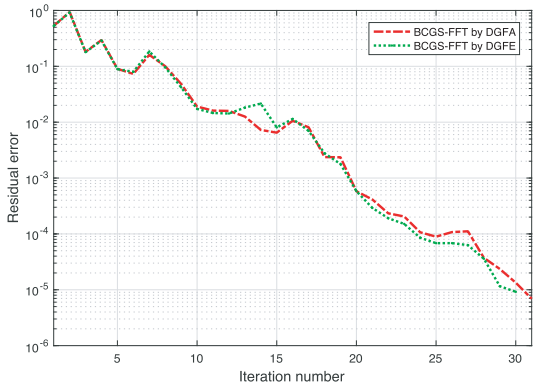

Fig. 4. BCGS-FFT iteration convergence curves for the two-layer uniaxial anisotropic cube.

where $\|\cdot\|$ denotes the L2-norm, $\mathbf{F}$ can be $\mathbf{E}$ or $\mathbf{H}$ which represents the electric field or the magnetic field, respectively. The subscripts b and c represent the BCGS method and the COMSOL simulations, respectively. The superscript g can either be e or a which means the field is computed by DGFE or DGFA, respectively.

Following the relative error defined earlier, we can easily acquire the total field errors as $err_E^a = 6.64\%$ and $err_E^e = 6.68\%$. Clearly, the total fields computed through DGFA and DGFE show the nearly perfect match and the errors between them are negligible. Fig. 4 shows the convergence curves of the BCGS-FFT method through DGFA and DGFE. The solver takes 31 and 30 iterations through DGFA and DGFE, respectively, when the relative residual errors become less than 10^{-5}. The computation consumption is 23 s and 180 MB memory when the DGFA is used and 24 s and 260 MB memory when DGFE is used. However, the COMSOL requires 808 s and 20 GB memory on the same machine. We can see that the BCGS-FFT solver using two kinds of DGFs has an obvious higher computation performance than the COMSOL simulations. When DGFE is adopted, the memory consumption is larger than that when DGFA is used in the BCGS-FFT method. All nine components of $\overline{\overline{\mathbf{G}}}_{\mathbf{E}}$ are involved in the BCGS iteration but only four components of $\overline{\overline{\mathbf{G}}}_{\mathbf{A}}$ are used. More memory is needed in the iteration when DGFE is taken.

B. Two-Layer Uniaxial Anisotropic Cylinder Embedded in the Middle Layer of a Three-Layer Medium

In this case, we challenge our algorithm and change the cubic scatterer to an object with the curved surface. We consider a two-layer concentric cylindrical scatterer embedded in the middle layer of a three-layer background medium. As shown in Fig. 5, the layer boundary positions are at $z = -0.4$ m and $z = 0.4$ m, respectively. The top layer is also air. The middle layer is uniaxial anisotropic and has the dielectric parameters

$$\overline{\overline{\varepsilon}}_b^2 = diag\{4.0, 4.0, 2.5\}, \overline{\overline{\sigma}}_b^2 = diag\{2, 2, 4\} \text{ mS/m} \quad (37)$$

and the bottom layer has the dielectric parameters

$$\overline{\overline{\varepsilon}}_b^3 = diag\{2.0, 2.0, 1.5\}, \overline{\overline{\sigma}}_b^3 = diag\{1, 1, 2\} \text{ mS/m}. \quad (38)$$

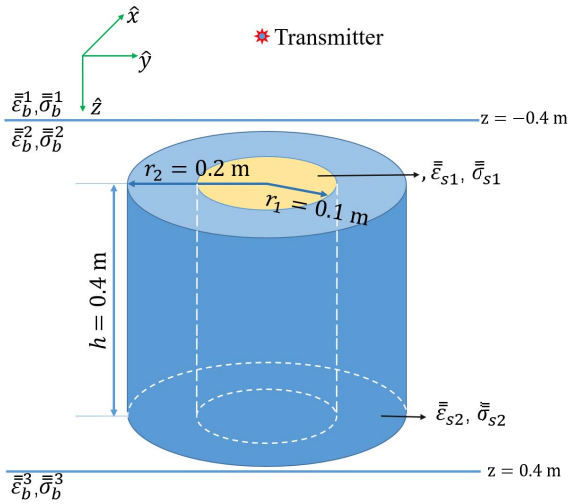

Fig. 5. Configuration of a two-layer concentric cylindrical scatterer with the radii $r_1 = 0.1$ m and $r_2 = 0.2$ m, and the height of $h = 0.4$ m embedded in the middle layer of a three-layer uniaxial anisotropic background medium.

The inner cylinder of the scatterer has the radius $r_1 = 0.1$ m, and the dielectric parameters are

$$\overline{\overline{\varepsilon}}_{s1} = diag\{2.5, 2.5, 2.0\}, \quad \overline{\overline{\sigma}}_{s1} = diag\{2, 2, 3\} \text{ mS/m}. \quad (39)$$

The outer cylinder of the scatterer has the radius $r_2 = 0.2$ m, and the dielectric parameters are

$$\overline{\overline{\varepsilon}}_{s2} = diag\{3.0, 3.0, 2.5\}, \quad \overline{\overline{\sigma}}_{s2} = diag\{3, 3, 4\} \text{ mS/m}. \quad (40)$$

The height of the concentric cylinder is $h = 0.4$ m and its center is located at (0, 0, 0) m. The electric dipole is located at (0, 0, −0.6) m. The computation domain of BCGS-FFT has the same size as that in last case and encloses the concentric cylinder. In this case, we study the discretization scheme effect on the computed total fields and convergence speed. Therefore, we discretize the computation domain into $50 \times 50 \times 50$ cells in the first scheme and $100 \times 100 \times 100$ cells in the second scheme. So, the SD is 18.75 PPW in the first scheme and 37.5 PPW in the second scheme. As shown in Fig. 6, the total electric fields solved in two discretization schemes match well. The fields solved through both DGFA and DGFE for SD = 18.75 and 37.5 PPW also match the COMSOL simulated results well. Here, we only show the x-component of the electric field. Other components have the same good fit and are not shown here. Fig. 7 shows the comparisons of BCGS iteration convergence curves for two discretization schemes. At the beginning of the BCGS iterations, the convergence curves have the same descending trends for different SD values. However, when the residual errors approach the threshold, the convergence curves are smoother for larger SD values. In addition, this is valid for the BCGS iterations using both DGFA and DGFE. The computation consumption of BCGS-FFT is 24 s and 190 MB for SD = 18.75 PPW and 116 s and 1.2 GB for SD = 37.5 PPW when DGFA is adopted. They are 25 s and 250 MB for SD = 18.75 PPW and 114 s and 1.7 GB for SD = 37.5 PPW when DGFE is used. However, the COMSOL needs

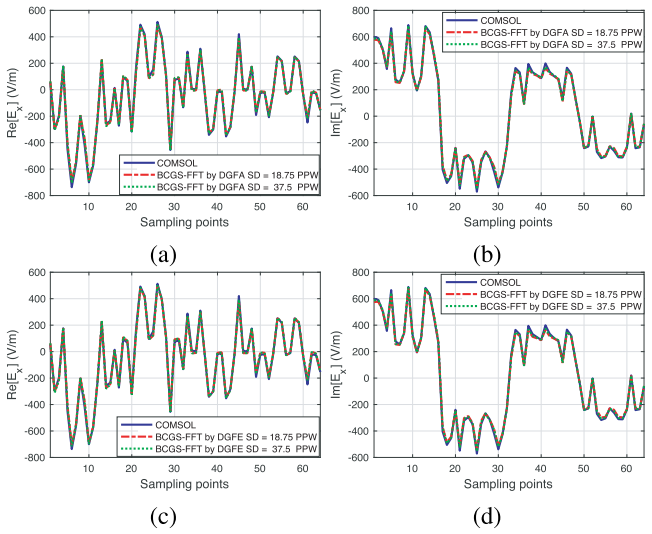

Fig. 6. Comparisons of the x-components of the total electric fields in the computation domain enclosing the concentric cylinder computed by the BCGS-FFT for two different discretization schemes and COMSOL simulations. (a) Real part by DGFA. (b) Imaginary part by DGFA. (c) Real part by DGFE. (d) Imaginary part by DGFE.

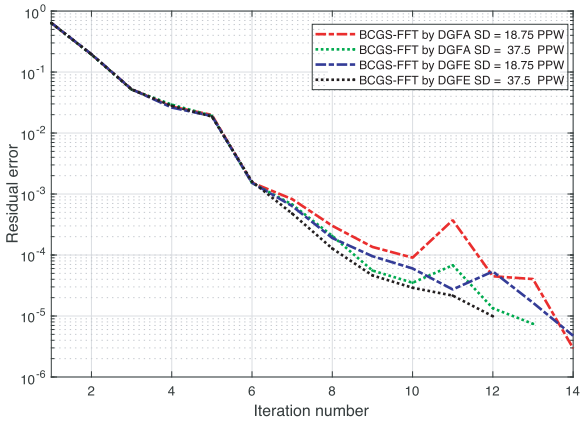

Fig. 7. BCGS-FFT iteration convergence curves for two different discretization schemes.

575 s and 13 GB memory on the same machine. Clearly, the larger SD scheme leads to more computation time and memory consumed although the BCGS iteration steps are almost the same in two discretization schemes.

C. Two-Layer Uniaxial Anisotropic Sphere in Embedded the Middle Layer of a Three-Layer Medium

In this case, we increase the electrical size of the scatterer and apply the BCGS-FFT method to compute the EM scattering of a two-layer sphere. It is assumed that a sphere with the inner radius $r_1 = 0.2$ m and outer radius $r_2 = 0.4$ m embedded in the middle layer of a three-layer background medium. As shown in Fig. 8, the layer boundary positions are at $z = -0.6$ m and $z = 0.6$ m, respectively. The top layer is also air. The middle layer is uniaxial anisotropic and has the dielectric parameters

$$\bar{\bar{\varepsilon}}_b^2 = diag\{2.0, 2.0, 1.5\}, \quad \bar{\bar{\sigma}}_b^2 = diag\{1, 1, 2\} \text{ mS/m} \quad (41)$$

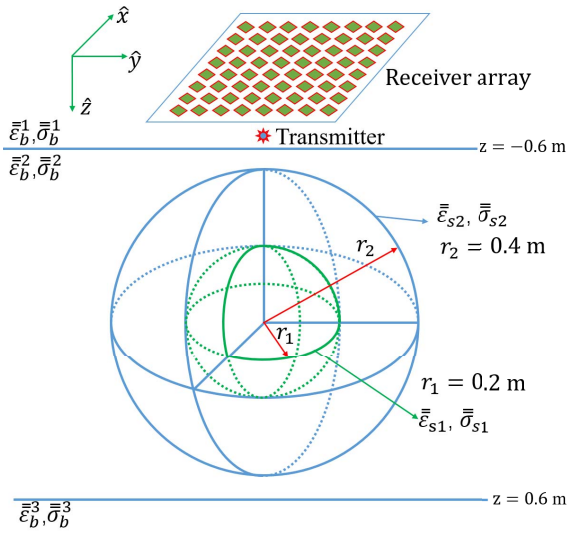

Fig. 8. Configuration of a two-layer sphere scatterer with the inner radius $r_1 = 0.2$ m and the outer radius $r_2 = 0.4$ m embedded in the middle layer of a three-layer uniaxial anisotropic background medium.

and the bottom layer has the dielectric parameters

$$\bar{\bar{\varepsilon}}_b^3 = diag\{4.0, 4.0, 2.5\}, \quad \bar{\bar{\sigma}}_b^3 = diag\{2, 2, 4\} \text{ mS/m}. \quad (42)$$

The inner sphere has the same dielectric parameters as those of the inner cylinder in last case while the outer sphere has the same dielectric parameters as those of the outer cylinder. Therefore, the diameter of the scatter is around 4.6λ, where λ is the smallest wavelength inside the two-layer sphere. The center of the sphere is located at (0, 0, 0) m. The computation domain of the BCGS-FFT solver is a cube with the size of 0.8 m $\times$ 0.8 m $\times$ 0.8 m which encloses the anisotropic two-layer sphere. It is discretized into 100^3 cubic cells with 3 million unknowns. The receiver array consists of 64 points and is located at the $z = -0.95$ m plane.

We first compare the total electric fields in 64 uniformly distributed sampling points inside the computation domain which encloses the two-layer sphere. As shown in Fig. 9, the total electric fields solved by BCGS-FFT through both DGFA and DGFE match the COMSOL simulations well. By using the relative error definition in (36), we can obtain the errors for the total fields as $err_E^a = 2.8\%$ and $err_E^e = 3.2\%$. In this case, the BCGS-FFT solver takes 152 s and 1.2 GB memory to complete the iteration when DGFA is used and 145 s and 1.7 GB memory when DGFE is used. However, the COMSOL simulation needs 1500 s and 23.6 GB memory.

Then, we compare the scattered electric and magnetic fields at the receiver array. The scattered electric fields are computed by (9) when the total fields in the computation domain are acquired by the BCGS-FFT iterations. The scattered magnetic fields are computed in a similar procedure but using the DGF in a layered uniaxial anisotropic medium for the magnetic field which can be found in [33]. Fig. 10 shows the comparisons of the z-component of the scattered electric and magnetic fields between our BCGS-FFT results and COMSOL simulations. Obviously, compared with the total fields shown in Fig. 9,

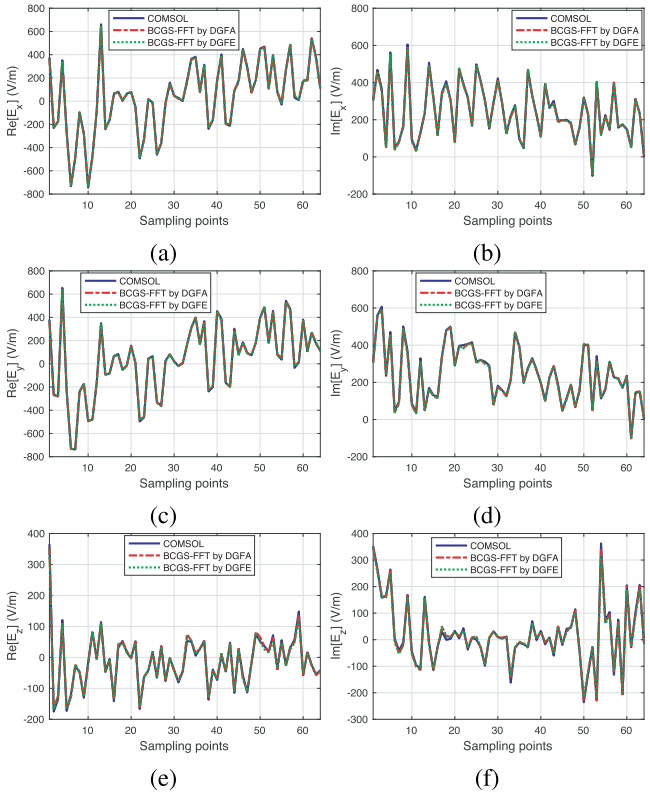

Fig. 9. Comparisons of the total electric fields inside the computation domain enclosing the two-layer sphere computed by the BCGS-FFT through DGFA as well as DGFE and simulated by the COMSOL. (a) Real part of E_x. (b) Imaginary part of E_x. (c) Real part of E_y. (d) Imaginary part of E_y. (e) Real part of E_z. (f) Imaginary part of E_z.

the relative errors of the scattered fields are larger. If we use the definition in (36), the errors for the scattered fields are $err_E^a = 15.1\%$, $err_E^e = 15.5\%$, $err_H^a = 15.1\%$, and $err_H^e = 15.6\%$. These larger errors are possibly due to the fact that the scattered fields are much smaller than the total fields at the receiver array and the computation accuracy of the COMSOL cannot be maintained during iterations for the scattered fields.

D. Two-Layer Uniaxial Anisotropic Sphere With Tilted Optical Axes Embedded in the Middle Layer of a Three-Layer Medium

In this subsection, the last case is repeated but it is assumed that the optical axes of the inner sphere and the outer sphere are tilted. We assume that the local coordinate system of the scatterer is aligned with the coordinate system of the background medium with the rotation transformation angles of $\psi_1 = 30°$ and $\psi_2 = 60°$ for the inner sphere but $\psi_1 = 60°$ and $\psi_2 = 120°$ for the outer sphere. By using the rotation transformation given in [34], we obtain the new dielectric parameter full tensors as

$$\overline{\overline{\varepsilon}}'_{s1} = \begin{bmatrix} 2.41 & -0.05 & -0.19 \\ -0.05 & 2.47 & -0.11 \\ -0.19 & -0.11 & 2.13 \end{bmatrix} \tag{43}$$

$$\overline{\overline{\sigma}}'_{s1} = \begin{bmatrix} 2.2 & 0.11 & 0.38 \\ 0.11 & 2.1 & 0.22 \\ 0.38 & 0.22 & 2.8 \end{bmatrix} \text{ mS/m} \tag{44}$$

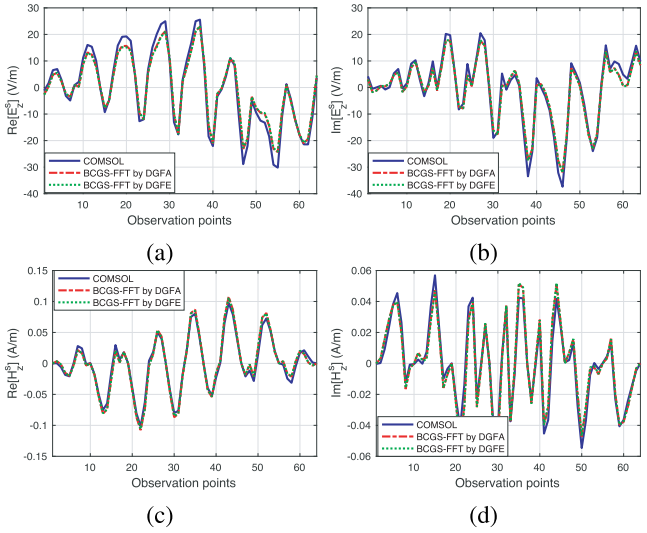

Fig. 10. Comparisons of the z-components of the scattered electric and magnetic fields at the receiver array computed by the BCGS-FFT through DGFA as well as DGFE and simulated by the COMSOL. (a) Real part of E_z^s. (b) Imaginary part of E_z^s. (c) Real part of H_z^s. (d) Imaginary part of H_z^s.

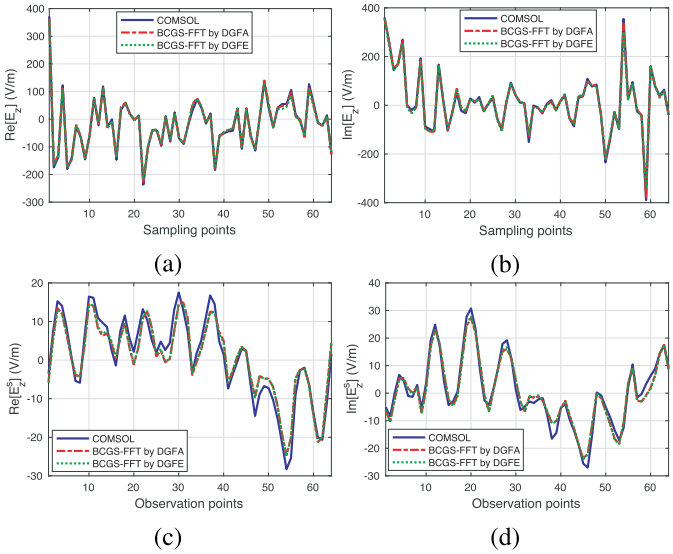

Fig. 11. Comparisons of the z-components of the total electric fields in the computation domain and the scattered electric fields at the receiver array when the optical axes of the sphere are tilted. (a) Real parts of total fields E_z. (b) Imaginary parts of total fields E_z. (c) Real parts of scattered fields E_z^s. (d) Imaginary parts of scattered fields E_z^s.

for the inner sphere and

$$\overline{\overline{\varepsilon}}'_{s2} = \begin{bmatrix} 2.7 & 0.16 & -0.19 \\ 0.16 & 2.9 & 0.11 \\ -0.19 & 0.11 & 2.9 \end{bmatrix} \tag{45}$$

$$\overline{\overline{\sigma}}'_{s2} = \begin{bmatrix} 3.6 & -0.32 & 0.38 \\ -0.32 & 3.2 & -0.22 \\ 0.38 & -0.22 & 3.3 \end{bmatrix} \text{ mS/m} \tag{46}$$

for the outer sphere.

Fig. 11 shows the comparisons of the z-components of total electric fields inside the computation domain and scattered electric fields at the receiver array. Comparisons for other

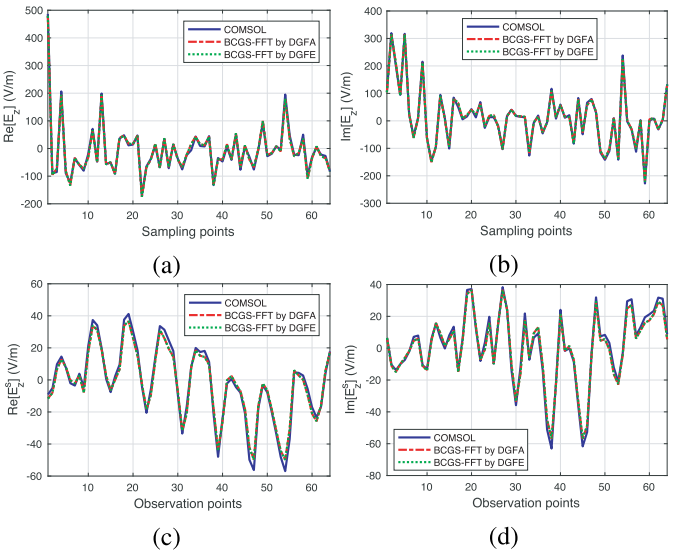

Fig. 12. Comparisons of the z-components of the total electric fields in the computation domain and the scattered electric fields at the receiver array for the isotropic EM scattering. (a) Real parts of total fields E_z. (b) Imaginary parts of total fields E_z. (c) Real parts of scattered fields E_z^s. (d) Imaginary parts of scattered fields E_z^s.

components are similar and not shown here. The relative error between the BCGS-FFT result and COMSOL simulation for the total field is $err_E^a = 2.8\%$ when DGFA is adopted, but $err_E^e = 3.5\%$ when DGFE is used. However, the relative errors for the scattered fields at the receiver array are $err_E^a = 19.5\%$, $err_E^e = 19.3\%$, $err_H^a = 19.3\%$, and $err_H^e = 19.1\%$, respectively. We can see that the total fields also have the good match between BCGS-FFT solutions and COMSOL simulations when the optical axes of the scatterers are rotated, but the errors of scattered fields become larger compared with those in last case. The computation time and the memory consumption of the COMSOL simulation are the same as in last case. However, the BCGS-FFT solver needs 170 s and 1.5 GB memory when DGFA is used and 180 s and 2 GB memory when DGFE is used. Clearly, more time and memory are consumed when the scatterer dielectric parameters are full tensors in BCGS-FFT solutions.

E. Comparisons With Isotropic EM Scattering

In this subsection, we compare the time and memory consumption as well as the computation accuracy between anisotropic and isotropic EM scattering. We also use the two-layer sphere model shown in last two subsections. However, in the isotropic EM scattering scenario, both the layered isotropic background medium and the scatterer have the dielectric constants same as the corresponding horizontal components given in Section III-C. For the layered isotropic background, the top layer is air, and $\varepsilon_b^2 = 2.0$, $\sigma_b^2 = 1$ mS/m, $\varepsilon_b^3 = 4.0$, and $\sigma_b^3 = 2$ mS/m. For the isotropic two-layer sphere, $\varepsilon_{s1} = 2.5$, $\sigma_{s1} = 2$ mS/m, and $\varepsilon_{s2} = 3.0$, $\sigma_{s2} = 3$ mS/m. Other configurations, including the transmitter, the receivers, and the discretization keep unchanged. Fig. 12 shows the representative z-component comparisons of the total electric fields inside the computation domain and the scattered electric fields at the receiver array for the isotropic EM scattering. The relative errors between the BCGS-FFT results and the COMSOL simulations for the total fields are 2.8% when either DGFA is adopted or DGFE is used. However, the relative errors for the scattered fields at the receiver array are $err_E^a = 14.3\%$, $err_E^e = 13.9\%$, $err_H^a = 14.1\%$, and $err_H^e = 13.8\%$, respectively. Compared with the errors presented in last two subsections, the errors of the total fields show little variation, but those of the scattered fields decrease obviously. The computation time and the memory consumption of the COMSOL simulation have no change compared with the two cases shown in last two subsections. However, the BCGS-FFT solver needs 144 s and 1.1 GB memory when DGFA is used and 137 s and 1.6 GB memory when DGFE is used. We can see that both the computation time and the memory consumption is lowered in the isotropic scattering case compared with these in the anisotropic case. This decrease is due to two reasons. One is the faster computation of DGFs in layered isotropic media compared to that in layered anisotropic media. The other is the more complicated implementation of BCGS-FFT when the scatterer has a full tensor contrast.

IV. Conclusion

In this paper, the BCGS-FFT fast algorithm is used to solve the discretized EFIE formulated for the EM scattering of uniaxial anisotropic objects embedded in a layered uniaxial background medium. In its iteration implementation, the discretized coefficients of the EFIE and the interactions between the DGFs and the equivalent current are different from those for EM scattering from scatterers in an isotropic background medium. The optical axis of the background medium is perpendicular to the layer boundaries. However, the optical axis of the scatterer can be tilted. The first-order volumetric rooftop basis functions are used to expand the electric flux density and the magnetic vector potential. Two types of DGFs, the DGFA and DGFE, are adopted to solve the discretized EFIE.

The performance of the proposed algorithm is validated by five numerical cases. In the BCGS iterations, the CPU time is reduced from $O(KN^2)$ to $O(KN\log N)$ by the use of the FFT algorithm, where N is the number of the unknowns. The computation accuracy is validated by the comparisons between the BCGS-FFT results and the COMSOL simulations. It shows that the proposed BCGS-FFT method is suitable for the computation of EM scattering of anisotropic objects embedded in layered uniaxial anisotropic media. The difference between the results computed through DGFA and DGFE is negligible. And, the convergence processes through two different DGFs are also similar. However, more computation time and memory are needed when DGFE is adopted than when DGFA is used, which is due to the fact that all the nine components of DGFE are involved in the BCGS iteration but only four components of DGFA are used. In addition, by comparing with the isotropic EM scattering case, we find that anisotropic scattering needs more memory and time in the BCGS-FFT implementation due to the more complicated DGF computation and the full tensor contrast of the scatterer.

Finally, we want to emphasize three points. First, this paper is limited to discussions of the scatterer with the uniaxial anisotropy. However, the mathematical derivation is also valid for scatterers with arbitrary anisotropy. The BCGS-FFT implementation for arbitrary anisotropic scatterers embedded in layered uniaxial background media is the same as that for the uniaxial scatterer with a tilted optical axis, which has been validated in Section III-D. Second, the contrast and anisotropy of the permeability are not included in this paper, i.e., the anisotropic magnetodielectric materials are not considered. The contrast of permeability will generate the equivalent magnetic current $\mathbf{M}_{eq}$ inside the scatterer and thus, the electric field vector potential $\mathbf{F}$ is added. Consequently, CFVIEs instead of the EFIE are required [28], [29]. In addition, (7) must be modified to account for the scattered electric field caused by $\mathbf{M}_{eq}$ and the more complicated relationship between vector and scalar potentials due to the uniaxial anisotropy of both the permittivity and permeability [33], which will finally affect the interaction between the $\nabla\nabla$ operator and the vector potentials expanded by the basis functions. Third, the BCGS-FFT fast solver proposed in this paper is not suitable for cross layer anisotropic scatterers. When the scatterers do not reside in a single layer, the DGFs cannot be decomposed into "minus" and "plus" parts anymore in the z direction, and thus, the FFT acceleration cannot be applied. A potential iteration solution for this cross layer scattering problem is given in the previous work [10]. However, these will be left as our future research work.

REFERENCES

[1] B. Wu, "Electromagnetic analysis of massive vertical interconnects for dense pin assignment optimization using multiple scattering technique," in *Proc. IEEE EMC/APEMC*, Singapore, May 2018, pp. 963–965.

[2] Q. H. Liu *et al.*, "Active microwave imaging. I. 2-D forward and inverse scattering methods," *IEEE Trans. Microw. Theory Techn.*, vol. 50, no. 1, pp. 123–133, Jan. 2002.

[3] C. Yu *et al.*, "Active microwave imaging II: 3-D system prototype and image reconstruction from experimental data," *IEEE Trans. Microw. Theory Techn.*, vol. 56, no. 4, pp. 991–1000, Apr. 2008.

[4] L. Tsang, K. H. Ding, S. Huang, and X. Xu, "Electromagnetic computation in scattering of electromagnetic waves by random rough surface and dense media in microwave remote sensing of land surfaces," *Proc. IEEE*, vol. 101, no. 2, pp. 255–279, Feb. 2012.

[5] C. Liu and L. C. Shen, "Numerical simulation of subsurface radar for detecting buried pipes," *IEEE Trans. Geosci. Remote Sens.*, vol. 29, no. 5, pp. 795–798, Sep. 1991.

[6] B. Liang *et al.*, "A new inversion method based on distorted born iterative method for grounded electrical source airborne transient electromagnetics," *IEEE Trans. Geosci. Remote Sens.*, vol. 56, no. 2, pp. 877–887, Feb. 2018.

[7] H. Liu, Z. Long, B. Tian, F. Han, G. Fang, and Q. H. Liu, "Two-dimensional reverse-time migration applied to GPR with a 3-D-to-2-D data conversion," *IEEE J. Sel. Topics Appl. Earth Observ. Remote Sens.*, vol. 10, no. 10, pp. 4313–4320, Oct. 2017.

[8] G. Bianconi, C. Pelletti, and R. Mittra, "A high-order characteristic basis function algorithm for an efficient analysis of printed microwave circuits and antennas etched on layered media," *IEEE Antennas Wireless Propag. Lett.*, vol. 12, pp. 543–546, 2013.

[9] H. Wang, P. So, S. Yang, W. J. R. Hoefer, and H. Du, "Numerical modeling of multicomponent induction well-logging tools in the cylindrically stratified anisotropic media," *IEEE Trans. Geosci. Remote Sens.*, vol. 46, no. 4, pp. 1134–1147, Apr. 2008.

[10] X. Millard and Q. H. Liu, "A fast volume integral equation solver for electromagnetic scattering from large inhomogeneous objects in planarly layered media," *IEEE Trans. Antennas Propag.*, vol. 51, no. 9, pp. 2393–2401, Sep. 2003.

[11] S. M. Rao, D. R. Wilton, and A. W. Glisson, "Electromagnetic scattering by surfaces of arbitrary shape," *IEEE Trans. Antennas Propag.*, vol. AP-30, no. 3, pp. 409–418, May 1982.

[12] L. E. Sun, "Electromagnetic modeling of inhomogeneous and anisotropic structures by volume integral equation methods," *Waves Random Complex Media*, vol. 25, no. 4, pp. 536–548, 2015.

[13] K. A. Michalski and D. Zheng, "Electromagnetic scattering and radiation by surfaces of arbitrary shape in layered media. I. Theory," *IEEE Trans. Antennas Propag.*, vol. 38, no. 3, pp. 335–344, Mar. 1990.

[14] K. A. Michalski and D. Zheng, "Electromagnetic scattering and radiation by surfaces of arbitrary shape in layered media. II. Implementation and results for contiguous half-spaces," *IEEE Trans. Antennas Propag.*, vol. 38, no. 3, pp. 345–352, Mar. 1990.

[15] X. M. Xu and Q. H. Liu, "The BCGS-FFT method for electromagnetic scattering from inhomogeneous objects in a planarly layered medium," *IEEE Antennas Wireless Propag. Lett.*, vol. 1, no. 1, pp. 77–80, 2002.

[16] D. V. Ginste, H. Rogier, F. Olyslager, and D. De Zutter, "A fast multipole method for layered media based on the application of perfectly matched layers—The 2-D case," *IEEE Trans. Antennas Propag.*, vol. 52, no. 10, pp. 2631–2640, Oct. 2004.

[17] M. S. Tong, Y. Q. Zhang, R. P. Chen, and C. X. Yang, "Fast solutions of volume integral equations for electromagnetic scattering by large highly anisotropic objects," *IEEE Trans. Antennas Propag.*, vol. 62, no. 7, pp. 1429–1436, Jul. 2014.

[18] X.-C. Nie, L.-W. Li, N. Yuan, T. S. Yeo, and Y.-B. Gan, "Precorrected-FFT solution of the volume Integral equation for 3-D inhomogeneous dielectric objects," *IEEE Trans. Antennas Propag.*, vol. 53, no. 1, pp. 313–320, Jan. 2005.

[19] L. Hu, L.-W. Li, and T.-S. Yeo, "Analysis of scattering by large inhomogeneous BI-anisotropic objects using AIM," *Progr. Electromagn. Res.*, vol. 99, pp. 21–36, 2009.

[20] K. Yang and A. E. Yılmaz, "A three-dimensional adaptive integral method for scattering from structures embedded in layered media," *IEEE Trans. Geosci. Remote Sens.*, vol. 50, no. 4, pp. 1130–1139, Apr. 2012.

[21] K. Yang and A. E. Yilmaz, "FFT-accelerated analysis of scattering from complex dielectrics embedded in uniaxial layered media," *IEEE Trans. Geosci. Remote Sens.*, vol. 10, no. 4, pp. 662–666, Jul. 2013.

[22] Z. Q. Zhang and Q. H. Liu, "Three-dimensional weak-form conjugate-and biconjugate-gradient FFT methods for volume integral equations," *Microw. Opt. Technol. Lett.*, vol. 29, no. 5, pp. 350–356, 2001.

[23] X. Xu, Q. H. Liu, and Z. Q. Zhang, "The stabilized biconjugate gradient fast Fourier transform method for electromagnetic scattering," *J. Appl. Computat. Electromag. Soc.*, vol. 17, no. 1, pp. 97–103, Mar. 2002.

[24] F. Li, Q. H. Liu, and L.-P. Song, "Three-dimensional reconstruction of objects buried in layered media using Born and distorted Born iterative methods," *IEEE Geosci. Remote Sens. Lett.*, vol. 1, no. 2, pp. 107–111, Apr. 2004.

[25] Y. Chen, P. Wen, F. Han, N. Liu, H. Liu, and Q. H. Liu, "Three-dimensional reconstruction of objects embedded in spherically layered media using variational born iterative method," *IEEE Geosci. Remote Sens. Lett.*, vol. 14, no. 7, pp. 1037–1041, Jul. 2017.

[26] X. Millard and Q. H. Liu, "Simulation of near-surface detection of objects in layered media by the BCGS-FFT method," *IEEE Trans. Geosci. Remote Sens.*, vol. 42, no. 2, pp. 327–334, Feb. 2004.

[27] W. Zhang and Q. H. Liu, "Three-dimensional scattering and inverse scattering from objects with simultaneous permittivity and permeability contrasts," *IEEE Trans. Geosci. Remote Sens.*, vol. 53, no. 1, pp. 429–439, Jan. 2015.

[28] Z. Yu, W. Zhang, and Q. H. Liu, "A mixed-order stabilized Bi-conjugate gradient FFT method for magnetodielectric objects," *IEEE Trans. Antennas Propag.*, vol. 62, no. 11, pp. 5647–5655, Nov. 2014.

[29] Z. Yu, W. Zhang, and Q. H. Liu, "The mixed-order BCGS-FFT method for the scattering of three-dimensional inhomogeneous anisotropic magnetodielectric objects," *IEEE Trans. Antennas Propag.*, vol. 63, no. 12, pp. 5709–5717, Dec. 2015.

[30] Y. Jia, Z. Yu, J. Dai, and Q. H. Liu, "Fast simulation of scattering problem for magnetodielectric materials with general anisotropy in layered media," *IEEE Trans. Antennas Propag.*, vol. 64, no. 11, pp. 4785–4793, Nov. 2016.

[31] Y. Zhong, P. P. Ding, M. Lambert, D. Lesselier, and X. Chen, "Fast calculation of scattering by 3-D inhomogeneities in uniaxial anisotropic multilayers," *IEEE Trans. Antennas Propag.*, vol. 62, no. 12, pp. 6365–6374, Dec. 2014.

[32] C. A. Balanis, *Advanced Engineering Electromagnetics*. New York, NY, USA: Wiley, 2012, ch. 7.

[33] K. A. Michalski and J. R. Mosig, "Multilayered media Green's functions in integral equation formulations," *IEEE Trans. Antennas Propag.*, vol. 45, no. 3, pp. 508–519, Mar. 1997.
[34] S. Mudaliar and J. K. Lee, "Dyadic Green's functions for a two-layer biaxially anisotropic medium," *J. Electromagn. Waves Appl.*, vol. 10, no. 7, pp. 909–923, 1996.
[35] J. Zhuo, F. Han, N. Liu, L. Ye, H. Liu, and Q. H. Liu, "Derivation and fast computation of dyadic Green's functions of magnetic vector potential for unbounded uniaxial anisotropic media," *Appl. Comput. Electromagn. Soc. J.*, vol. 32, no. 10, pp. 862–870, 2017.
[36] W. S. Weiglhofer, "Dyadic Green's functions for general uniaxial media," *IEE Proc. H-Microw., Antennas Propag.*, vol. 137, no. 1, pp. 5–20, Feb. 1990.
[37] A. Abubakar and T. M. Habashy, "A closed-form expression of the electromagnetic tensor Green's functions for a homogeneous TI-anisotropic medium," *IEEE Geosci. Remote Sens. Lett.*, vol. 3, no. 4, pp. 447–451, Oct. 2006.
[38] P. Zwamborn and P. M. van den Berg, "The three dimensional weak form of the conjugate gradient FFT method for solving scattering problems," *IEEE Trans. Microw. Theory Techn.*, vol. 40, no. 9, pp. 1757–1766, Sep. 1992.
[39] D. E. Livesay and K. Chen, "Electromagnetic fields induced inside arbitrarily shaped biological bodies," *IEEE Trans. Microw. Theory Techn.*, vol. MTT-22, no. 12, pp. 1273–1280, Dec. 1974.
[40] A. D. Yaghjian, "Electric dyadic Green's functions in the source region," *Proc. IEEE*, vol. 68, no. 2, pp. 248–263, Feb. 1980.
[41] L. Tsang, J. A. Kong, K.-H. Ding, and C. O. Ao, *Scattering of Electromagnetic Waves: Numerical Simulations*. New York, NY, USA: Wiley, 2001, ch. 2.
[42] A. Lakhtakia and W. S. Weiglhofer, "Time-harmonic electromagnetic field in a source region in a uniaxial dielectric-magnetic medium," *Int. J. Appl. Electromagn. Mech.*, vol. 8, no. 2, pp. 167–177, 1997.

Feng Han (M'17) received the B.S. degree in electronic science from Beijing Normal University, Beijing, China, in 2003, the M.S. degree in geophysics from Peking University, Beijing, in 2006, and the Ph.D. degree in electrical engineering from Duke University, Durham, NC, USA, in 2011.

He is currently an Assistant Professor with the Institute of Electromagnetics and Acoustics, Xiamen University, Xiamen, China. His current research interests include ionosphere remote sensing by radio atmospherics, electromagnetic full-wave inversion by integral equations, reverse time migration image, and the design of an electromagnetic detection system.

Jianliang Zhuo received the B.S. degree in communication engineering and business administration and the M.S. degree in communication and information system from the University of Electronic Science and Technology of China, Chengdu, China, in 2007 and 2011, respectively. He is currently pursuing the Ph.D. degree with Xiamen University, Xiamen, China.

His current research interests include fast-forward solvers in electromagnetics and inverse scattering methods for microelectronics and RF systems.

Na Liu (M'18) received the Ph.D. degree in computational mathematics from the University of Chinese Academy of Sciences, Beijing, China, in 2013.

From 2012 to 2013, she was a Visiting Student with the Department of Electrical and Computer Engineering, Duke University, Durham, NC, USA. From 2013 to 2017, she held a post-doctoral position at Xiamen University, Xiamen, China, where she is currently an Associate Professor with the Institute of Electromagnetics and Acoustics. Her current research interests include computational electromagnetics, especially the fast and efficient methods for complex media and their applications in cavities and optical waveguide problems.

Yanhui Liu (M'15) received the B.S. and Ph.D. degrees in electrical engineering from the University of Electronic Science and Technology of China, Chengdu, China, in 2004 and 2009, respectively.

From 2007 to 2009, he was a Visiting Scholar with the Department of Electrical Engineering, Duke University, Durham, NC, USA. Since 2011, he has been with Xiamen University, Xiamen, China, where he is currently a Full Professor with the Department of Electronic Science. He has authored or coauthored over 90 peer-reviewed journal and conference papers. He holds several granted Chinese patents. His current research interests include antenna array design, array signal processing, and microwave imaging methods.

Hai Liu (S'11–M'13) received the B.E. and M.E. degrees in civil engineering from Tongji University, Shanghai, China, in 2007 and 2009, respectively, and the Ph.D. degree in environmental studies from Tohoku University, Sendai, Japan, in 2013.

From 2013 to 2014, he was a Research Fellow with the Center for Northeast Asian Studies, Tohoku University. From 2014 to 2017, he was an Assistant Professor with the Institute of Electromagnetics and Acoustics, Xiamen University, Xiamen, China. He is currently an Associate Professor with the School of Civil Engineering, Guangzhou University, Guangzhou, China. His current research interests include the development of ground-penetrating radar systems and algorithms for a wide variety of applications, such as nondestructive testing in civil engineering, environmental monitoring, archeological investigation, and lunar exploration.

Qing Huo Liu (S'88–M'89–SM'94–F'05) received the B.S. and M.S. degrees in physics from Xiamen University, Xiamen, China, and the Ph.D. degree in electrical engineering from the University of Illinois at Urbana–Champaign, Champaign, IL, USA.

From 1986 to 1988, he was a Research Assistant with the Electromagnetics Laboratory, University of Illinois at Urbana–Champaign, where he was as a Post-Doctoral Research Associate from 1989 to 1990. He was a Research Scientist and the Program Leader with Schlumberger-Doll Research, Ridgefield, CT, USA, from 1990 to1995. From 1996 to 1999, he was an Associate Professor with New Mexico State University, Las Cruces, NM, USA. Since 1999, he has been with Duke University, Durham, NC, USA, where he is currently a Professor of electrical and computer engineering. He has published over 400 papers in refereed journals and 500 papers in conference proceedings. His current research interests include computational electromagnetics and acoustics, inverse problems, and their application in nanophotonics, geophysics, biomedical imaging, and electronic packaging.

Dr. Liu is a fellow of the Acoustical Society of America, the Electromagnetics Academy, and the Optical Society of America. He currently serves as the Founding Editor-in-Chief for the new IEEE JOURNAL ON MULTISCALE AND MULTIPHYSICS COMPUTATIONAL TECHNIQUES, the Deputy Editor-in-Chief for *Progress in Electromagnetics Research*, an Associate Editor for the IEEE TRANSACTIONS ON GEOSCIENCE AND REMOTE SENSING, and an Editor for the *Journal of Computational Acoustics*.